

See discussions, stats, and author profiles for this publication at: <https://www.researchgate.net/publication/263944249>

A Theory for the Morphological Dependence of Wetting on a Physically Patterned Solid Surface

ARTICLE *in* LANGMUIR · SEPTEMBER 2012

Impact Factor: 4.46 · DOI: 10.1021/la3026304

CITATIONS

15

READS

20

3 AUTHORS, INCLUDING:



[Azar Shahraz](#)

11 PUBLICATIONS 63 CITATIONS

SEE PROFILE



[Ali Borhan](#)

Pennsylvania State University

108 PUBLICATIONS 642 CITATIONS

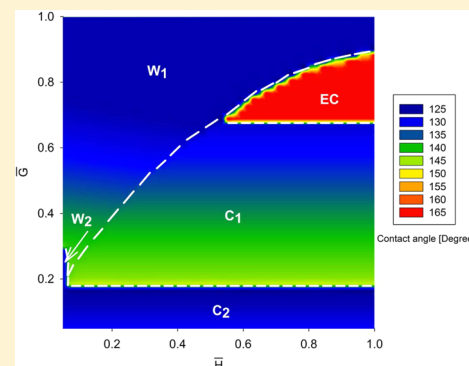
SEE PROFILE

A Theory for the Morphological Dependence of Wetting on a Physically Patterned Solid Surface

Azar Shahraz,[†] Ali Borhan,[†] and Kristen A. Fichthorn^{*,†,‡}

[†]Department of Chemical Engineering, and [‡]Department of Physics, The Pennsylvania State University, University Park, Pennsylvania 16802, United States

ABSTRACT: We present a theoretical model for predicting equilibrium wetting configurations of two-dimensional droplets on periodically grooved hydrophobic surfaces. The main advantage of our model is that it accounts for pinning/depinning of the contact line at step edges, a feature that is not captured by the Cassie and Wenzel models. We also account for the effects of gravity (via the Bond number) on various wetting configurations that can occur. Using free-energy minimization, we construct phase diagrams depicting the dependence of the wetting modes (including the number of surface grooves involved in the wetting configuration) and their corresponding contact angles on the geometrical parameters characterizing the patterned surface. In the limit of vanishing Bond number, the predicted wetting modes and contact angles become independent of drop size if the geometrical parameters are scaled with drop radius. Contact angles predicted by our continuum-level theoretical model are in good agreement with corresponding results from nanometer-scale molecular dynamics simulations. Our theoretical predictions are also in good agreement with experimentally measured contact angles of small drops, for which gravitational effects on interface deformation are negligible. We show that contact-line pinning is important for superhydrophobicity and that the contact angle is maximized when the droplet size is comparable to the length scale of the surface pattern.



INTRODUCTION

The ability to create surfaces with controlled wettability is important for a wide variety of applications. Superhydrophobic surfaces, which possess a high ($>150^\circ$) contact angle for water droplets and low ($<10^\circ$) contact-angle hysteresis, have a number of beneficial properties, including water repellency, self-cleaning, low drag, and antifouling characteristics.^{1,2} An archetypical, biologically inspired surface for superhydrophobicity is the Lotus leaf. The success of the Lotus leaf at water repellency and self-cleaning is attributed to its chemical composition, as well as its surface structure, which is characterized by roughness over both micrometer and submicrometer length scales.^{3–6} The idea that (multiscale) surface roughness can induce superhydrophobicity has inspired many studies aimed at synthesizing rough or patterned surfaces with superhydrophobic properties^{1,2,5–12} and quantifying the effect of roughness on superhydrophobicity.^{13–22}

Wetting on structured surfaces is typically classified by one of two models. In the Wenzel, or noncomposite, model,²³ liquid fills all of the surface asperities beneath the droplet. Another possible wetting state is described by the Cassie–Baxter, or composite, model,²⁴ in which the droplet is lifted up by surface roughness, with air pockets in the asperities underneath it. In addition to qualitatively describing wetting modes, both of these models can be employed to predict contact angles on rough surfaces based on geometrical roughness parameters and the contact angle for a flat surface made of the same material as the rough one. However, experimental studies have shown that

these models can only describe contact angles for a limited range of surface morphologies.^{21,25–27} Gao and McCarthy argued that the Wenzel and Cassie equations are not directly relevant to water repellency and that events at the contact line, not over the liquid–solid interfacial area, control the contact angle.¹⁸ In molecular dynamics (MD) simulations of droplet wetting on patterned surfaces, both Cassie and Wenzel wetting modes have been observed; however, the contact angles in these simulations tend to exhibit poor agreement with those predicted by the Cassie and Wenzel models.^{28,29} Additionally, other wetting modes can occur that are not predicted by the Cassie and Wenzel models. These include a “mixed” mode, in which liquid partially fills the surface asperities^{29–31} and, as we will discuss below, the “epitaxial Cassie” mode, an experimentally observed wetting state in which a droplet rests on top of a single asperity.^{32,33}

In the design of superhydrophobic surfaces, it is important to be able to predict the wetting mode, contact angle, and contact-angle hysteresis that will occur for a given surface morphology. Such a prediction is complicated by experimental observations of multiple wetting states and contact angles on a given surface.^{13,14,17,22} These experimental studies indicate that wetting can involve local free-energy minima, in addition to the global-minimum wetting state. Droplets can remain in local

Received: June 29, 2012

Revised: August 20, 2012

Published: September 21, 2012

minima over experimental time scales due to free-energy barriers that hinder attainment of the global-minimum wetting state. Theoretical studies based on continuum^{34–42} and atomic-scale^{43,44} approaches have been performed to elucidate wetting transitions and free-energy barriers between the Cassie and Wenzel states. In their numerical studies of droplets on a grooved substrate using the Surface Evolver software, Chen and co-workers found multiple wetting states corresponding to different numbers of pillars underneath the droplet.⁴¹

Among the possible local minimum wetting states for a given surface morphology, there exists a global minimum, and it is important to be able to predict this state. Many prior theoretical efforts to predict wetting free-energy minima have been based on the Wenzel or Cassie–Baxter models^{35,45,46} and/or incorporate the assumption that the drop is large as compared to the surface roughness.^{36,37} Detailed numerical simulations have been performed to solve for the droplet wetting mode and shape on various patterned surfaces.^{41,42} However, despite these studies, basic questions persist in efforts to design surfaces with optimal superhydrophobicity.

In this study, we present a model that predicts the global-minimum wetting modes of a two-dimensional droplet on a grooved surface. Unlike the Cassie and Wenzel models, our model accounts for pinning of the contact line, which is important for achieving superhydrophobicity. We also account for the effects of gravity on droplet wetting via the Bond number. As we will discuss below, our model reproduces, both qualitatively and quantitatively, many experimentally observed features of droplet wetting on patterned surfaces. We conduct analogous molecular-dynamics (MD) simulations of droplet wetting on grooved surfaces. In the limit of zero Bond number, our model exhibits good agreement with the MD simulations. Below, we discuss our model.

MODEL FORMULATION

We consider a cylindrical liquid droplet on a patterned solid surface characterized by the periodic, rectangular grooves shown in Figure 1. The grooves have width G and height H and

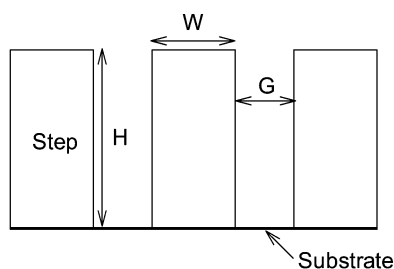


Figure 1. View of the model grooved surface in the direction parallel to the grooves. The surface topology is characterized by groove width G , groove height H , and a step width W .

are separated by steps of width W . To simplify the problem, we consider the droplet to be of infinite length along the cylindrical axis, which is aligned with the grooves, so that the problem becomes two-dimensional. We also assume that the drop has a constant-curvature profile in the cross section perpendicular to the grooves (i.e., the drop profile is a portion of a circle). The assumption of constant-curvature profile is valid provided the drop is sufficiently small that its shape is not affected by gravity.⁴⁷ As we will discuss below, this assumption is validated by comparison to MD simulations.

We consider four different wetting modes, which are shown in Figure 2. These include the Cassie and Wenzel modes, as well as the epitaxial Cassie state, an experimentally observed^{32,33} wetting mode in which a droplet resides completely on top of a single step. We also consider the possibility of a mixed mode, which is defined as a wetting configuration in which the droplet partially penetrates and forms a meniscus within the grooves.

In each of the wetting modes in Figure 2, the free-energy difference per unit length (ΔE) between a system consisting of a droplet on the patterned surface and a surface without a droplet is given by

$$\Delta E = A_{lv}\sigma_{lv} + A_{sl}(\sigma_{sl} - \sigma_{sv}) + F_g \quad (1)$$

where the first two terms represent interfacial energies and the third term F_g reflects the effect of gravity. In eq 1, A_{lv} is the area per axial length of the liquid–vapor interface, A_{sl} is the area per axial length of the solid–liquid interface, and σ_{lv} , σ_{sl} , and σ_{sv} denote the liquid–vapor, solid–liquid, and solid–vapor interfacial energies, respectively. The expressions for A_{lv} , A_{sl} , and F_g depend on the wetting mode. To illustrate our approach, we consider a droplet that covers one surface groove in the Cassie mode. A schematic for this wetting mode is shown in Figure 3.

For the droplet in Figure 3, the liquid–vapor interfacial area (per unit axial length), A_{lv} , is the sum of the area (per unit axial length) of the cylindrical cap resting on top of the pillars and that of the flat interface over the groove. This is given by

$$A_{lv} = 2R\theta + G \quad (2)$$

where R is the radius of curvature of the cylindrical cap (see Figure 3). The liquid–solid interfacial area per unit axial length, A_{sl} , can be written as

$$A_{sl} = 2R \sin \theta - G \quad (3)$$

The gravitational energy contribution per unit axial length, F_g , is given by

$$F_g = \pi \rho g R_0^2 z_0 \quad (4)$$

where z_0 is the elevation of the center of mass of the droplet relative to the surface of the substrate, ρ is the liquid density, g is the gravitational acceleration, and R_0 is the cylindrical-equivalent radius of the drop. By substituting eqs 2–4 into eq 1 and recognizing that the static equilibrium contact angle on the analogous flat surface, θ_e , is related to the interfacial energies through Young's equation, that is, $\sigma_{lv} \cos \theta_e = \sigma_{sv} - \sigma_{sl}$, the free energy difference per unit axial length for the configuration shown in Figure 1 can be rewritten as

$$\Delta E = [2R(\theta - \cos \theta_e \sin \theta) + G(1 + \cos \theta_e)]\sigma_{lv} + \pi \rho g R_0^2 z_0 \quad (5)$$

where z_0 is given by

$$z_0 = H - R \cos \theta + \frac{2R^3 \sin^3 \theta}{3\pi R_0^2} \quad (6)$$

and the radius of curvature R can be related to drop size R_0 and contact angle θ according to

$$R = R_0 \left(\frac{\pi}{\theta - \sin \theta \cos \theta} \right)^{1/2} \quad (7)$$

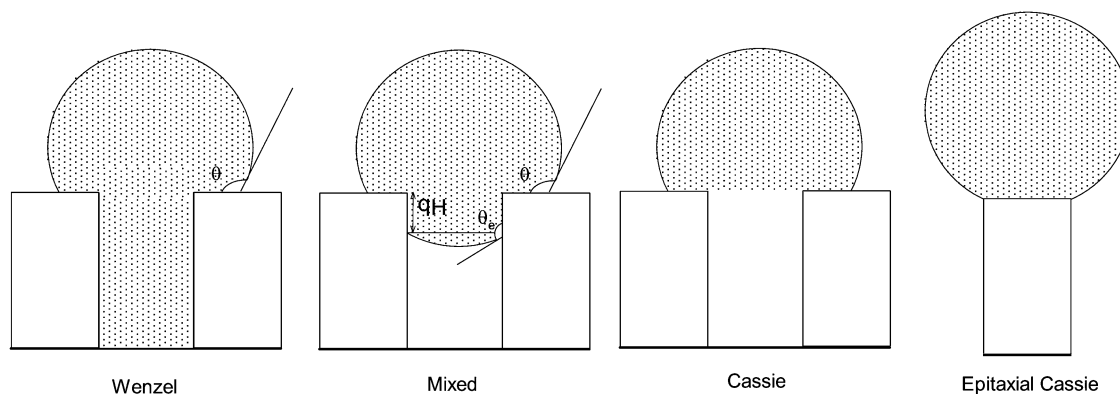


Figure 2. Various wetting modes considered in this study. θ is the apparent contact angle, θ_e is the equilibrium contact angle for the droplet on a flat surface made of the same material as the grooved surface, and q is the fraction of the height of the groove that is filled with liquid.

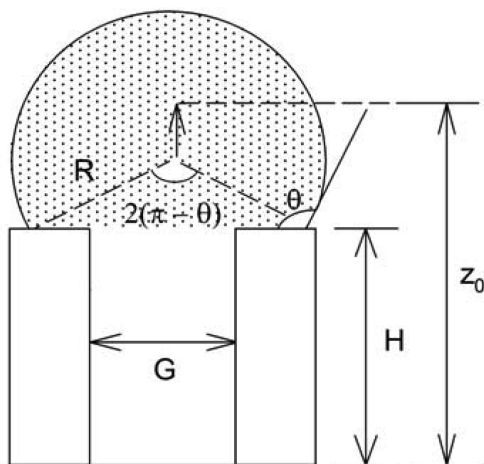


Figure 3. Schematic of a droplet in the Cassie state with one groove underneath it. G and H are the width and height of the groove, respectively, R is the radius of curvature of the droplet, θ is the equilibrium contact angle, and z_0 is the elevation of the droplet center of mass relative to the substrate surface.

Specific expressions for the free energies of the wetting configurations in Figure 2 are presented below. In what follows, all lengths and energies (per unit axial length) are made dimensionless with R_0 and $\sigma_{lv}R_0$, respectively, and all dimensionless variables are designated by overbars (i.e., $\bar{H} = H/R_0$, $\bar{W} = W/R_0$, $\bar{G} = G/R_0$, $\bar{R} = R/R_0$, and $\bar{\Delta E} = \Delta E/\sigma_{lv}R_0$). In addition, the subscripts W, C, M, and EC refer to the Wenzel, Cassie, mixed, and epitaxial Cassie modes, respectively.

Cassie mode:

$$\bar{\Delta E}_C = 2\bar{R}_C(\theta - \cos \theta_e \sin \theta) + n\bar{G}(1 + \cos \theta_e) + Bo \left[\frac{2}{3}\bar{R}_C^3 \sin^3 \theta + \pi(\bar{H} - \bar{R}_C \cos \theta) \right] \quad (8)$$

where n is the number of grooves underneath the droplet, $Bo = \rho g R_0^2 / \sigma_{lv}$ is the Bond number, and \bar{R}_C , the dimensionless radius of curvature of the cylindrical portion of the drop that lies above the steps, is given by

$$\bar{R}_C = \left(\frac{\pi}{\theta - \sin \theta \cos \theta} \right)^{1/2} \quad (9)$$

For $n = 1$, the dimensionless free-energy difference in eq 8 is the same as that for our example in Figure 3 and eq 5.

Wenzel mode:

$$\bar{\Delta E}_W = 2\bar{R}_W(\theta - \cos \theta_e \sin \theta) - 2n\bar{H} \cos \theta_e + Bo \left[\frac{2}{3}\bar{R}_W^3 \sin^3 \theta + (\pi - n\bar{G}\bar{H})(\bar{H} - \bar{R}_W \cos \theta) + \frac{1}{2}n\bar{G}\bar{H}^2 \right] \quad (10)$$

where

$$\bar{R}_W = \left(\frac{\pi - n\bar{G}\bar{H}}{\theta - \sin \theta \cos \theta} \right)^{1/2} \quad (11)$$

Mixed mode:

$$\begin{aligned} \bar{\Delta E}_M = & 2\bar{R}_M(\theta - \cos \theta_e \sin \theta) + n\bar{G}[(\pi/2 - \theta_e) \sec \theta_e \\ & + \cos \theta_e] - 2nq\bar{H} \cos \theta_e \\ & + Bo \left[\frac{2}{3}\bar{R}_M^3 \sin^3 \theta + \bar{R}_M^2(\bar{H} - \bar{R}_M \cos \theta) \right. \\ & \left. (\theta - \sin \theta \cos \theta) \right] \\ & + \frac{n}{4}Bo\bar{G}^2 \left\{ \sec^2 \theta_e (\theta_e + \sin \theta_e \cos \theta_e - \pi/2) \right. \\ & \left. \left[(1 - q)\bar{H} - \frac{1}{2}\bar{G} \tan \theta_e \right] - \frac{1}{3}\bar{G} \right\} \\ & + nBo(1 - q/2)q\bar{G}\bar{H}^2 \end{aligned} \quad (12)$$

where

$$\bar{R}_M = \left\{ \frac{\pi - \frac{n}{4}\bar{G}^2[(\theta_e - \pi/2) \tan^2 \theta_e + \tan \theta_e + \theta_e - \pi/2] - nq\bar{G}\bar{H}}{\theta - \sin \theta \cos \theta} \right\}^{1/2} \quad (13)$$

and q is the fraction of the groove that is filled with liquid. For this configuration, the contact angle formed by the meniscus within the groove at the solid wall is θ_e .

Epitaxial Cassie mode:

$$\bar{\Delta E}_{EC} = 2\bar{R}_{EC}(\theta - \cos \theta_e \sin \theta) + Bo \left[\frac{2}{3}\bar{R}_{EC}^3 \sin^3 \theta + \pi(\bar{H} - \bar{R}_{EC} \cos \theta) \right] \quad (14)$$

where

$$\bar{R}_{EC} = \left(\frac{\pi}{\theta - \sin \theta \cos \theta} \right)^{1/2} \quad (15)$$

The apparent contact angle for each wetting mode is obtained by minimizing the corresponding energy expression with respect to θ , subject to the constraint that the contact line be located on top of a step and not over a groove. When the contact line is not pinned at the edge of a step (i.e., it is free to move), minimizing the free-energy expressions for different wetting modes of a droplet covering n grooves yields the following expression for the contact angle θ_j^f , where j refers to the wetting mode, which could be C, W, M, or EC:

$$\begin{aligned} & 2(\cos \theta_j^f - \cos \theta_e)(\theta_j^f \cos \theta_j^f - \sin \theta_j^f)(\theta_j^f - \sin \theta_j^f \cos \theta_j^f) \\ & + Bo \bar{R}_j^2 (\theta_j^f - \sin \theta_j^f \cos \theta_j^f)(-2 \sin^3 \theta_j^f \\ & + \theta_j^f \sin^2 \theta_j^f \cos \theta_j^f + \theta_j^{f2} \sin \theta_j^f) = 0 \end{aligned} \quad (16)$$

Here, $\bar{R}_j(\theta_j^f)$ is the dimensionless radius of curvature of the cylindrical cap that lies above the steps, given by eqs 9, 11, 13, and 15 for the different modes. In the limit $Bo \rightarrow 0$, which occurs for sufficiently small drops, eq 16 simplifies to

$$\begin{aligned} & (\cos \theta_j^f - \cos \theta_e)(\theta_j^f \cos \theta_j^f - \sin \theta_j^f)(\theta_j^f - \sin \theta_j^f \cos \theta_j^f) \\ & = 0 \end{aligned} \quad (17)$$

whose only nontrivial solution in the range $[0, \pi]$ is $\theta_j^f = \theta_e$. Thus, for $Bo = 0$, if the contact line resides on top of a step without being pinned at the step edges, the droplet will maintain the same contact angle as that on a flat surface, regardless of the wetting mode.

In the general case, eq 16 can be solved numerically to find θ_j^f for a given droplet configuration. Frequently, the solution to this equation leads to the situation where the contact line resides above a groove, in which case we consider that it has to be pinned at a step edge. There are two different scenarios for contact-line pinning, and these are shown in Figure 4. In the

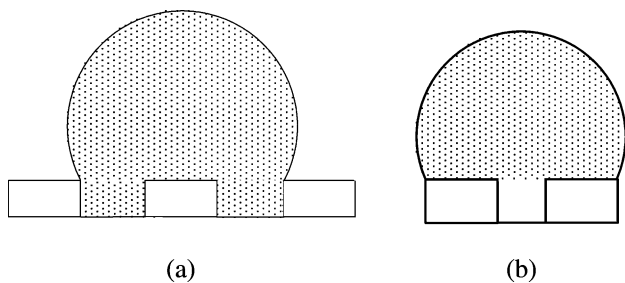


Figure 4. Two scenarios for contact-line pinning at step edges: (a) the droplet periphery resides over grooves and (b) the droplet periphery resides over steps.

first scenario shown in Figure 4a, which can occur for $n \geq 1$, the basal length of the drop (with contact angle θ_j^f from eq 16) is smaller than $(n - 1)\bar{W} + n\bar{G}$. In this case, the minimum free energy will be achieved when the contact line is pinned at a step edge, with the droplet periphery over grooves so that the drop covers n grooves and $(n - 1)$ steps. The resulting contact angle θ_j^{ps} is then obtained from the solution of

$$2\bar{R}_j \sin \theta_j^{ps} = (n - 1)\bar{W} + n\bar{G} \quad (18)$$

where $\bar{R}_j(\theta_j^{ps})$ is given by eqs 9, 11, and 13 for the different modes.

Similarly, if the resulting basal length of the drop (with contact angle θ_j^f from eq 16) exceeds $(n + 1)\bar{W} + n\bar{G}$, the minimum free energy will be achieved when the contact line is pinned at a step edge, with the droplet periphery over steps so that the droplet covers $(n + 1)$ steps and n grooves [cf., Figure 4b]. The resulting contact angle θ_j^{ps} is obtained from the solution of

$$2\bar{R}_j \sin \theta_j^{ps} = (n + 1)\bar{W} + n\bar{G} \quad (19)$$

where $\bar{R}_j(\theta_j^{ps})$ is given by eqs 9, 11, 13, and 15 for the different modes. We note that this scenario also holds for $n \geq 0$, so the epitaxial Cassie mode ($n = 0$) falls under this case.

For a given surface topology, the equilibrium contact angle is the one corresponding to the minimum free energy among all possible wetting modes and number of grooves involved in the wetting configuration. We find the global minimum in free energy using the approach illustrated in Figure 5, wherein the

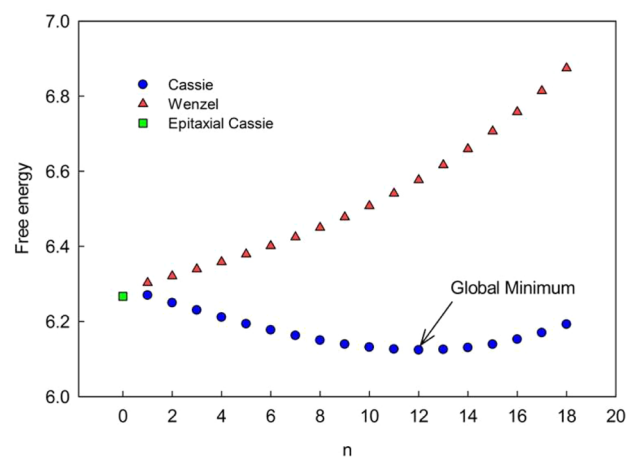


Figure 5. The dimensionless free energy of a drop with $R_0 = 0.25$ mm, $Bo = 0.00084$, and $\theta_e = 126^\circ$ as a function of the number of grooves n beneath the drop on a surface with $\bar{H} = \bar{G} = \bar{W} = 0.05$.

minimum free energies are plotted for different configurations of a water droplet with $R_0 = 0.25$ mm and $\theta_e = 126^\circ$ on a fixed surface topology with $\bar{H} = \bar{G} = \bar{W} = 0.05$. To obtain each point on Figure 5, we used a bisection algorithm to solve eq 16 for the contact angle that minimizes the free energy. If in the resulting configuration the contact line lies above a groove, we use eq 18 or eq 19, as discussed above, to find the contact angle that yields the minimum free energy for a pinned configuration. The results in this figure show that the Cassie mode with $n = 12$ represents the global free-energy-minimum configuration in this case.

We note that no points are shown for the mixed mode in Figure 5. This is because, for every case considered in our study, we found that the mixed mode was never the minimum-energy configuration. For $Bo = 0$, we found that the mixed mode cannot represent a global minimum in free energy for any value of $0 < q < 1$ because, for fixed surface topology, ΔE_M does not have a local minimum, that is, $(\partial \Delta E_M) / (\partial q) \neq 0$ for $0 < q < 1$. We also did not observe the mixed mode in any of the corresponding MD simulations that we will discuss below. The mixed mode has been observed in MD^{29,30} and lattice Boltzmann simulations³¹ of droplets on surfaces patterned with square pillars. Apparently, this wetting mode is sensitive to

details of the surface geometry. Thus, we exclude the mixed mode in our discussion below.

RESULTS AND DISCUSSION

Below, we present various predictions of our model. In most of the discussion below, we focus on the limit of vanishing Bond number, for which the effects of gravity are unimportant. The small Bond-number limit is of interest for many applications, including electrowetting, microfluidic devices, and Lab-on-a-Chip systems.^{48–50} The zero Bond-number limit is also appropriate for comparing our results to those from classical MD simulations, and we present such a comparison below. We include a discussion on the influence of gravity (finite Bo) on droplet configurations and wetting modes. We also include a comparison of our model predictions to experiment, for experiments in which the drop sizes span a range including both small and finite Bond numbers.

Contact Angle Discontinuity. One of the interesting features of surface roughness is that it introduces discontinuities in the apparent contact angle as the droplet size or surface topology is varied in a systematic way. These discontinuities are due to both wetting-mode transitions and pinning/depinning transitions of the contact line. To illustrate this point, we consider the case of $Bo = 0$, for which gravity does not play a significant role.

The apparent contact angle for the wetting mode with the minimum free energy is plotted as a function of \bar{G} in Figure 6,

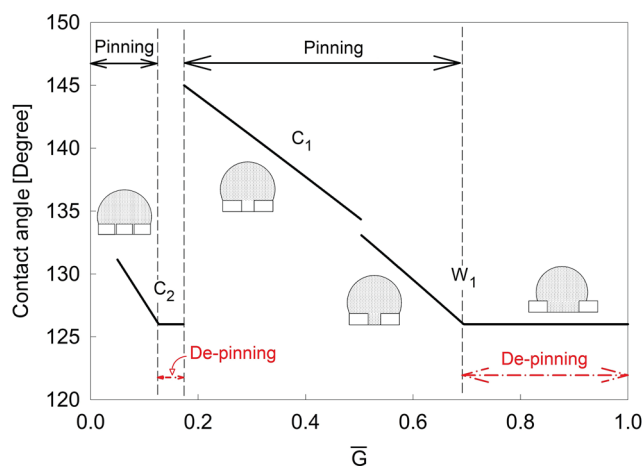


Figure 6. The apparent contact angle as a function of \bar{G} for constant \bar{H} ($=0.3$) and \bar{W} ($=0.5$) for $Bo = 0$. Discontinuities in the contact angle result from pinning/depinning transitions, as well as from wetting-mode transitions.

for fixed values of $\bar{W} = 0.5$ and $\bar{H} = 0.3$. Each equilibrium wetting state in Figure 6 is identified by a letter indicating the wetting mode, followed by a number denoting the number of grooves beneath the droplet. The W_1 configuration, in which the droplet is in the Wenzel state with one liquid-filled groove beneath it, occurs for the largest values of \bar{G} . For $\bar{G} > 0.695$, the contact line is depinned in the W_1 state, so that $\theta = \theta_e = 126^\circ$. As the grooves become narrower, the contact lines move toward the step edges with constant apparent contact angle until contact-line pinning occurs at $\bar{G} = 0.695$. While the contact lines remain pinned, the apparent contact angle increases with decreasing groove width, because it is energetically unfavorable for the drop to reduce its contact angle by jumping across a groove. As the groove width decreases further,

a discontinuity in the apparent contact angle eventually appears due to a wetting-mode change from W_1 to C_1 , followed by a much larger second discontinuity associated with the transition from C_1 to C_2 . The apparent contact angle is reduced sharply to θ_e when it becomes energetically favorable for the droplet to cover two grooves. In the C_2 state, contact-line pinning occurs again as \bar{G} is reduced below 0.127, and the apparent contact angle increases with decreasing groove width.

Equilibrium Wetting States. One interesting feature of our model in the limit of small Bond numbers is that the apparent contact angle and the equilibrium wetting state of a droplet are not affected by droplet size when the geometrical parameters of the surface are scaled with R_0 . This is apparent from inspection of eqs 8–14 and is also illustrated in Table 1,

Table 1. Effect of the Bond Number on the Wetting Mode and Apparent Contact Angle θ of a Droplet (with $\theta_e = 126^\circ$) for Different Scaled Surface Topologies

| Bo | $\bar{G} = \bar{W} = \bar{H} = 0.1$ | | $\bar{G} = 0.15, \bar{W} = 0.1, \bar{H} = 0.05$ | | $\bar{G} = \bar{W} = \bar{H} = 0.01$ | |
|--------|-------------------------------------|--------------|---|--------------|--------------------------------------|--------------|
| | θ° | wetting mode | θ° | wetting mode | θ° | wetting mode |
| 0.0014 | 141 | C_6 | 139 | W_5 | 143 | C_{62} |
| 0.0030 | 141 | C_6 | 139 | W_5 | 143 | C_{62} |
| 0.0054 | 141 | C_6 | 139 | W_5 | 143 | C_{62} |
| 0.0216 | 141 | C_6 | 139 | W_5 | 141 | C_{64} |
| 0.0487 | 141 | C_6 | 139 | W_5 | 140 | C_{66} |
| 0.0865 | 141 | C_6 | 139 | W_5 | 138 | C_{69} |
| 0.1351 | 134 | C_7 | 139 | W_5 | 136 | C_{72} |
| 0.2112 | 134 | C_7 | 131 | W_6 | 133 | C_{77} |
| 0.3041 | 128 | C_8 | 131 | W_6 | 129 | C_{83} |

which lists wetting modes and contact angles for droplets as a function of the Bond number. The entries in Table 1 can be interpreted as a series of experiments on different surfaces in which the drop size is increased along with the geometrical parameters describing the surface topology, such that \bar{G} , \bar{H} , and \bar{W} remain constant. These results show that the contact angle and wetting mode remain constant and independent of drop size for sufficiently small Bond numbers (drop sizes). As the Bond number (drop size) increases beyond a threshold that depends on surface geometry, the influence of gravity becomes significant, and the contact angles and wetting modes become dependent on drop size. As we shall elaborate below, the drop-size independence of the wetting mode/contact angle for scaled surface geometries indicates that nanoscale MD simulations can be used to predict wetting behavior for droplet sizes and surface topologies beyond the nanometer scale (for which this technique is typically used).

To explore the full range of wetting behavior predicted by our model, we construct wetting phase diagrams illustrating droplet wetting modes and apparent contact angles as a function of \bar{H} , \bar{W} , and \bar{G} in the small Bond-number limit. Figures 7 and 8 show cross sections of the wetting phase diagram for two different values of \bar{W} on hydrophobic surfaces with $\theta_e = 126^\circ$ and $\theta_e = 115^\circ$. These phase diagrams show that the Wenzel mode is energetically favorable for large groove widths and small step heights. In these surface geometries, the energetically unfavorable interaction of the droplet with the groove walls is minimized. Conversely, the Cassie mode is favored for narrower and/or taller grooves. The contact angle is independent of groove height in all of the Cassie configurations.

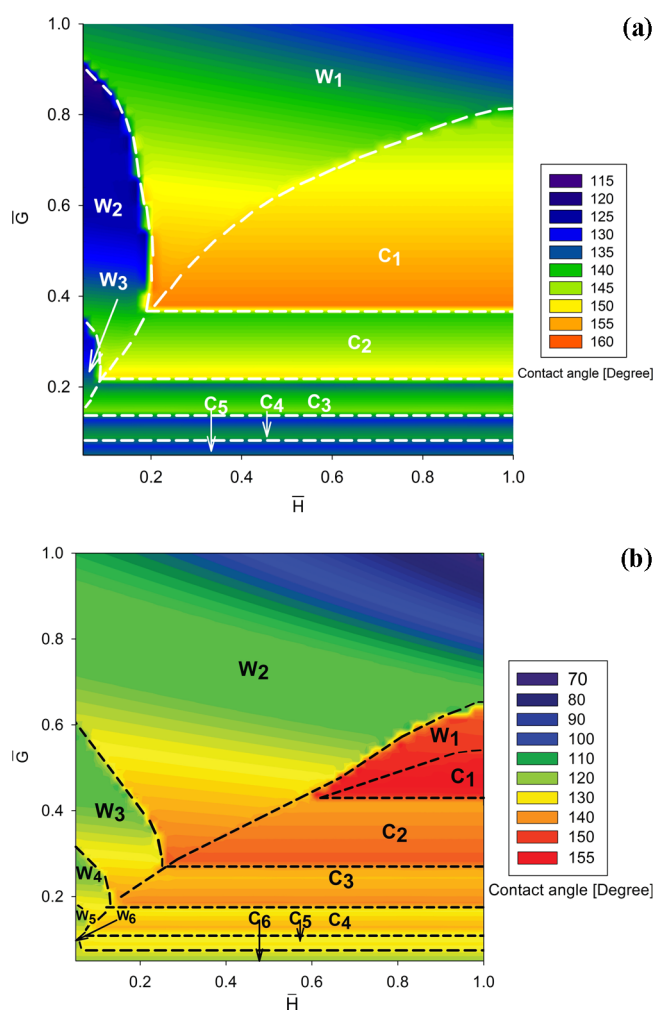


Figure 7. Cross-section of the wetting phase diagram for two different hydrophobic surfaces, $\theta_e = 126^\circ$ (a) and $\theta_e = 115^\circ$ (b), with fixed $\bar{W} = 0.2$ and $Bo = 0$.

The epitaxial Cassie (EC) mode becomes the lowest-energy state when the dimensions of the groove pattern become comparable to drop size. This occurs with $\theta_e = 126^\circ$ for wide steps (relative to the droplet's basal length) separated by sufficiently high and wide grooves that inhibit the droplet from bridging a single groove.

The phase diagrams for the two values of θ_e are qualitatively similar, although with decreasing θ_e , the boundary separating the Wenzel and Cassie modes shifts to lower \bar{G} . This shift can be understood as resulting from the more favorable liquid–solid interaction with lower θ_e , which creates less of an energetic penalty for liquid to reside within the grooves. Within the Wenzel and Cassie regions, we see a wider range of wetting configurations with larger values of n (e.g., W_4 , W_5 , and C_6) with decreasing θ_e . This shift to larger n can be understood in terms of the increasing basal area of the drop with lower θ_e . The boundaries of the epitaxial Cassie region are shifted to larger values of \bar{W} as the value of θ_e is reduced. As a result, the epitaxial Cassie region disappears for $\bar{W} = 0.5$ over the range of parameters shown in Figure 8b, but it can be recovered by increasing the step width to $\bar{W} \geq 0.9$.

Defining a superhydrophobic surface as one for which the contact angle is larger than 150° , the results in Figure 7 show that for $\bar{W} = 0.2$, most of the topological region corresponding

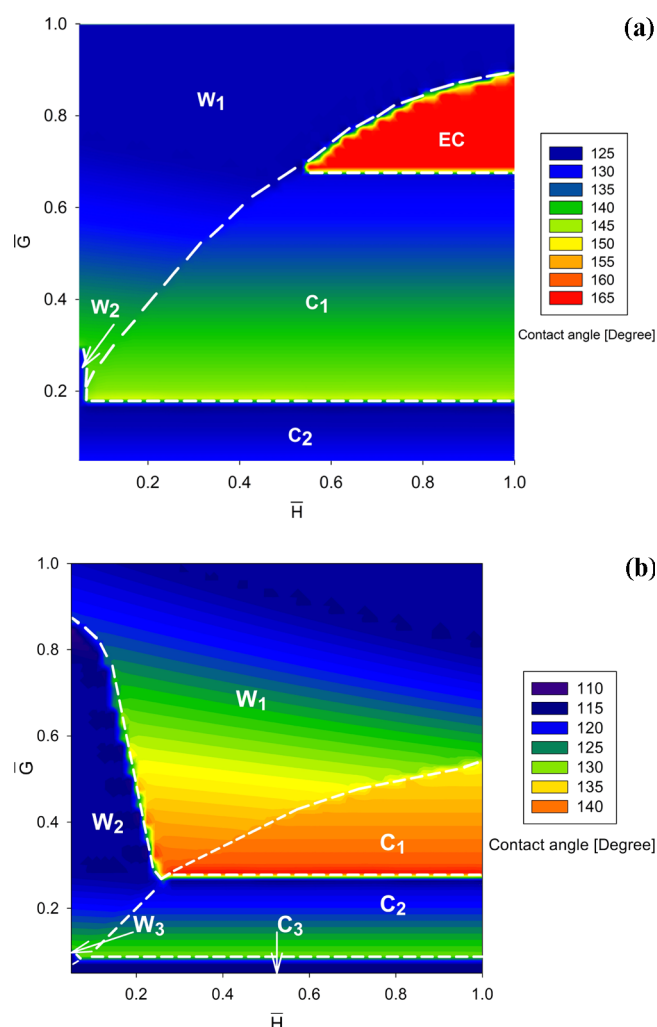


Figure 8. Cross-section of the wetting phase diagram for two different hydrophobic surfaces, $\theta_e = 126^\circ$ (a) and $\theta_e = 115^\circ$ (b), with fixed $\bar{W} = 0.5$ and $Bo = 0$.

to the C_1 wetting mode, as well as portions of the W_1 and C_2 domains, are superhydrophobic. For wider steps, the EC mode is superhydrophobic in Figure 8a, and the contact angles associated with this mode are in the same range as those for water on the Lotus leaf.^{3,4} In all of these wetting modes (and especially in the EC mode), the droplet rests on a relatively small number of steps, so its size is comparable to the length scale of the surface pattern. This finding is in line with results from the MD simulation study of Yang, Tartaglino, and Persson, who probed liquid droplets in contact with self-affine fractal surfaces and found that long-wavelength roughness plays an important role in determining the contact angle.²⁸ Our results may provide an indication of why multiple-scale roughness, that reaches droplet size scales, has been observed in conjunction with superhydrophobicity.^{2,3,5}

Although most of the contact angles reported in Figures 7 and 8 are greater than θ_e , there are regions in the phase diagram [e.g., portions of the W_2 region in Figures 7 and 8b] where the contact angle is less than θ_e . These regions tend to be characterized by wide grooves relative to the droplet size. Here, the grooves have a sufficiently large volume-to-wall-area ratio that a significant amount of liquid can reside in them. For the W_2 wetting mode [cf., Figure 7b], this reduces the volume of the drop that resides above the groove to the point that there is

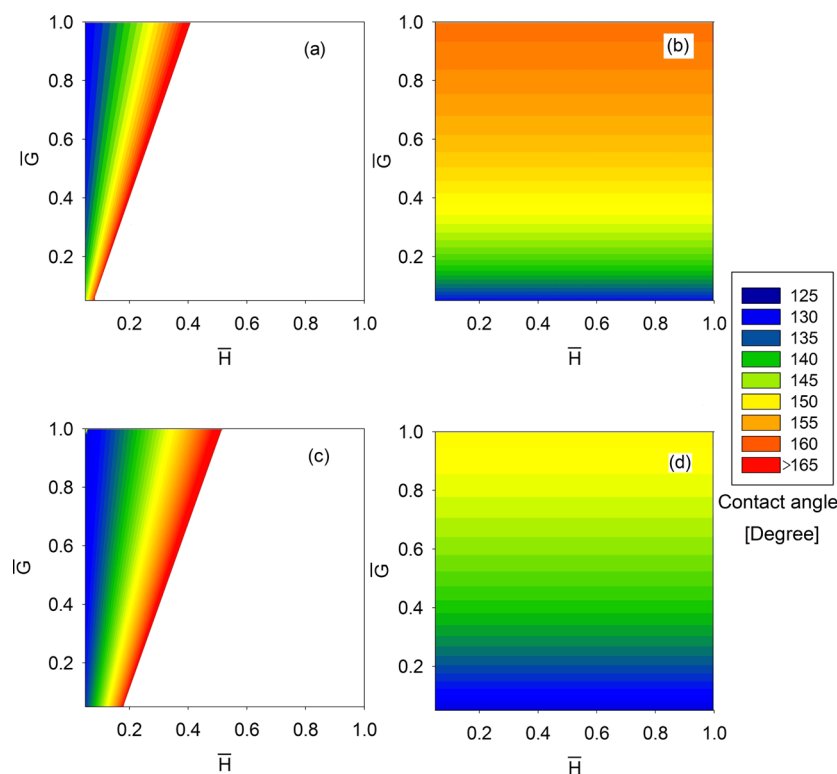


Figure 9. Contact-angle isocontours with $\theta_e = 126^\circ$ based on the Wenzel and Cassie models for two step widths: (a) Wenzel model, $\bar{W} = 0.2$, (b) Cassie model, $\bar{W} = 0.2$, (c) Wenzel model, $\bar{W} = 0.5$, and (d) Cassie model, $\bar{W} = 0.5$.

not sufficient liquid to produce a cylindrical cap with a contact angle of θ_e . A similar argument applies for the W_2 configuration [in Figures 7a and 8b] where droplets with $\theta < \theta_e$ lie close to the W_2 – W_1 boundary. Here, the decrease in the liquid–vapor interfacial energy in going from a W_1 configuration to a W_2 configuration more than compensates for the increase in the solid–liquid interfacial energy, thereby resulting in a lower energy for the W_2 configuration. The resulting W_2 configuration has a lower contact angle than θ_e because the volume of the cylindrical cap above the grooves is not sufficient to have θ_e .

Comparison to Cassie and Wenzel Models. Contact-angle isocontours based on the Cassie and Wenzel models are presented in Figure 9 for $\theta_e = 126^\circ$ and two step widths of $\bar{W} = 0.2$ and $\bar{W} = 0.5$. These correspond to the wetting phase diagrams of our model shown in Figures 7a and 8a. In the Cassie model, the apparent contact angle θ_C is given by

$$\cos \theta_C = \Phi(1 + \cos \theta_e) - 1 \quad (20)$$

where $\Phi = 1 - G/(W + G)$. The apparent contact angle from the Wenzel model, θ_W , is given by

$$\cos \theta_W = f_r \cos \theta_e \quad (21)$$

where $f_r = 1 + 2H/(W + G)$.

As shown in Figure 9, the Wenzel model is only applicable over a small portion of the \bar{G} – \bar{H} domain, which roughly coincides with the region where we observe the Wenzel wetting mode in our model. However, for large \bar{G} , our model predicts the Wenzel mode for a larger range of \bar{H} than is seen for the Wenzel model. Equation 21 yields contact angles that increase monotonically with \bar{H} for a fixed value of \bar{G} , and predicts superhydrophobic contact angles ($>150^\circ$). In contrast, our model shows only a weak dependence of the contact angle on \bar{H} for a fixed \bar{G} , unless a wetting-mode boundary is crossed, in

which case the contact angle varies discontinuously with \bar{H} due to contact-line pinning. The Wenzel contact angles from our model do not tend to fall within the superhydrophobic range.

The Cassie model predicts that the contact angle is independent of groove height and that it increases monotonically with increasing groove width. Although our model also shows that the contact angle is independent of groove height, it exhibits discontinuities associated with contact-line pinning as the wetting modes change (e.g., from C_1 to C_2). The Cassie model does not predict the epitaxial Cassie mode, which we find for wide steps, as shown in Figure 8a. As compared to the Cassie and Wenzel models, the main advantages of our model are that it provides a detailed description of wetting modes (e.g., we distinguish W_1 from W_2) and it accounts for pinning/depinning of the contact line at step edges. Such effects are not taken into account in the Cassie and Wenzel models.

■ COMPARISON TO MD SIMULATIONS

To validate the predictions of our model, we compared them to classical MD simulations of analogous molecular systems. MD was employed in the constant number, volume, and temperature (NVT) ensemble to simulate wetting of a periodically grooved solid surface by an infinitely long (periodic) cylindrical Lennard-Jones liquid droplet consisting of more than 12 000 atoms. Preliminary results from these simulations are presented in ref 30, which contains more details of the simulation methods. A difference from ref 30 is that, in the MD simulations presented in this Article, we employ a coarse-grained potential for the liquid–surface interaction that we developed recently.⁵¹ For zero Bond number, which occurs in the MD simulations, correspondence between the model and molecular-level simulations can be achieved if θ_e and scaled parameters of the surface topology are the same in the two

descriptions. To determine the correct equilibrium wetting mode for a given set of surface topological parameters in the MD simulations, three different initial droplet configurations (i.e., Cassie, Wenzel, and epitaxial Cassie) were considered. MD simulations beginning with droplets in each of these modes were run for 10 ns, and the wetting mode and contact angle were obtained as averages from 10 different simulation snapshots over the final 2 ns of each run. For the small (~ 10 nm radius) droplets considered in the MD simulations, we found that the equilibrium drop profiles have constant curvature, in good agreement with the assumption of a circular profile in our model. Thus, we obtained equilibrium contact angles using the apex height and basal length of the best-fit circular profile for the droplet.⁵² We determine these dimensions by calculating the density profile in the droplet and defining the liquid–vapor interface using the maximum-gradient method.⁵³

Figure 10 shows a comparison between the wetting modes observed in the MD simulations and those predicted by the

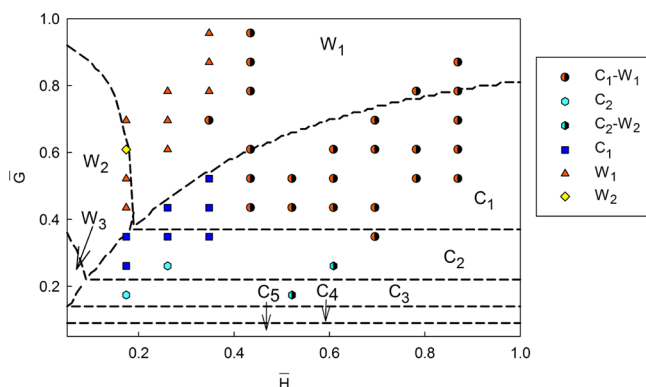


Figure 10. A comparison between the predictions of mathematical model [phase boundaries between various wetting modes (e.g., W_1) delineated by dashed lines] and MD simulations (symbols) in a cross-section of the phase diagram for $\theta_e = 126^\circ$, $\bar{W} = 0.2$, and $Bo = 0$. Symbols with more than one wetting mode listed for them represent instances of multiple wetting modes, in which the observed wetting mode depends on the initial configuration.

macroscopic model in a cut of the wetting phase diagram. Here, we see that the phase boundaries predicted by the mathematical model are roughly consistent with the wetting modes observed in MD simulations. Unlike the model, our MD simulations predict multiple wetting modes for the same surface topology in some cases. We note that multiple wetting modes have been observed experimentally for the same surface topography.^{13,14,17,22} It should be noted that the wetting modes observed in the MD simulations are not necessarily global equilibrium configurations, as free-energy barriers can hinder transitions between metastable and stable wetting states. Thus, in the multiple wetting states observed for different initial conditions in the MD simulations, some states are metastable and some are true global minima. Nevertheless, we see in Figure 10 that in most of the cases for which the MD simulations exhibit multiple wetting modes, the stable wetting mode predicted by the model is also observed in MD.

In Figure 11, we compare the contact angles from the MD simulations in Figure 10 to those from the model for those MD simulations in which the observed wetting mode is the same as that predicted by the model. The quantitative agreement between the contact angles predicted by the macroscopic

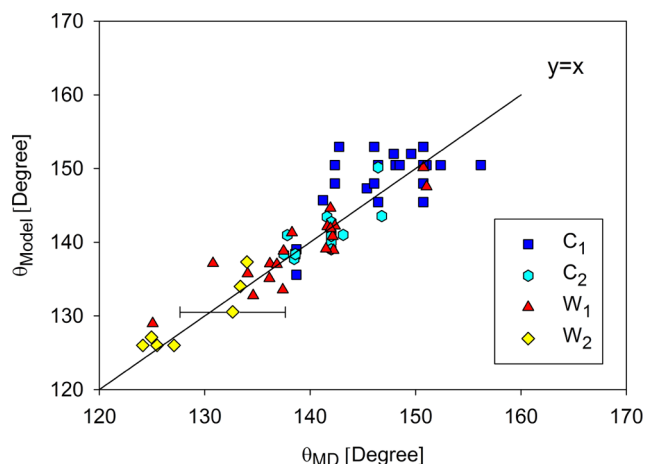


Figure 11. The difference between theoretically predicted contact angles θ_{model} and those obtained from MD simulations θ_{MD} , for different droplet wetting states. The uncertainty in each of the MD contact angles is $\pm 5^\circ$, as indicated by the error bar on one of the points.

model and those resulting from MD simulations is sufficiently good (with most differences between the two falling within the uncertainty of the MD simulations) to indicate that the model provides a useful representation of wetting.

Influence of Gravity. We now turn our attention to the influence of gravity, which becomes increasingly important as the Bond number increases, as was shown in Table 1. In Table 2, we compare the predicted wetting modes and contact angles of water droplets ($\rho = 997 \text{ kg/m}^3$ and $\sigma_{lv} = 72.3 \times 10^{-3} \text{ N/m}$) of different sizes to those for the zero-Bond-number ($g = 0$) counterparts. A comparison of the results for $Bo = 0$ to those for non-zero Bond number indicates that droplets with radii as large as several hundred micrometers can fall within the small Bond-number limit. The effect of gravity becomes significant when the droplet radius exceeds a threshold value that depends on the surface geometry. We find that the threshold radius decreases with decreasing size of the surface features. For example, the threshold radius decreases from 0.735 ± 0.005 mm for $G = H = W = 0.1$ mm to 0.400 ± 0.005 mm for $G = H = W = 0.01$ mm. Once the threshold radius is reached, the droplet assumes an extended surface configuration, in which it covers an increasing number of surface grooves and possesses decreasingly smaller apparent contact angles as its size increases. As the Bond number increases further, we expect the interplay between gravity and interfacial energy to lead to a flattening of the droplet profile, such that the droplet no longer has a constant-curvature cross-section.⁴⁷ Such deformation effects are not included in our model.

Comparison to Experiment. To further confirm the validity of our theoretical analysis, we compared our model predictions to available experimental data for droplet wetting on grooved solid surfaces fabricated from a relatively hydrophobic material (ppHex, with $\theta_e = 100^\circ$), with a fixed groove height of $3 \text{ }\mu\text{m}$ and equally sized groove and step widths of 5, 10, 25, and $100 \text{ }\mu\text{m}$.⁵⁴ In this study, wetting is anisotropic, and apparent contact angles were measured from optical images obtained in the directions parallel and perpendicular to the grooves. Because our theoretical model is two-dimensional and assumes the droplet to be infinitely long in the direction parallel to the grooves, we compare our predictions to experimental

Table 2. Effect of Gravity on the Wetting State and Contact Angle θ of a Droplet on a Grooved Surface

| R_0 (mm) | $G = W = H = 0.1$ (mm) | | | | $G = 0.15, W = 0.1, H = 0.05$ (mm) | | | | $G = W = H = 0.01$ (mm) | | | |
|---------------|------------------------|--------------|----------------|--------------------------|------------------------------------|--------------|----------------|--------------------------|-------------------------|--------------|----------------|--------------------------|
| | θ° | wetting mode | θ° | wetting mode ($g = 0$) | θ° | wetting mode | θ° | wetting mode ($g = 0$) | θ° | wetting mode | θ° | wetting mode ($g = 0$) |
| 0.1 | 126 | W_3 | 126 | W_3 | 126 | W_3 | 126 | W_3 | 141 | C_6 | 141 | C_6 |
| 0.15 | 161 | EC | 161 | EC | 126 | W_1 | 126 | W_1 | 142 | C_9 | 142 | C_9 |
| 0.2 | 134 | C_1 | 134 | C_1 | 126 | W_1 | 126 | W_1 | 143 | C_{12} | 143 | C_{12} |
| 0.4 | 143 | C_2 | 143 | C_2 | 134 | W_2 | 134 | W_2 | 142 | C_{25} | 142 | C_{25} |
| 0.6 | 145 | C_3 | 145 | C_3 | 137 | W_3 | 137 | W_3 | 140 | C_{39} | 143 | C_{37} |
| 0.8 | 138 | C_5 | 146 | C_4 | 138 | W_4 | 138 | W_4 | 139 | C_{54} | 142 | C_{50} |
| 1.0 | 134 | C_7 | 141 | C_6 | 139 | W_5 | 139 | W_5 | 136 | C_{72} | 143 | C_{62} |
| 1.25 | 134 | C_9 | 144 | C_7 | 135 | W_7 | 141 | W_6 | 132 | C_{97} | 142 | C_{78} |
| 1.5 | 129 | C_{12} | 142 | C_9 | 126 | W_{10} | 143 | W_7 | 128 | C_{126} | 142 | C_{94} |

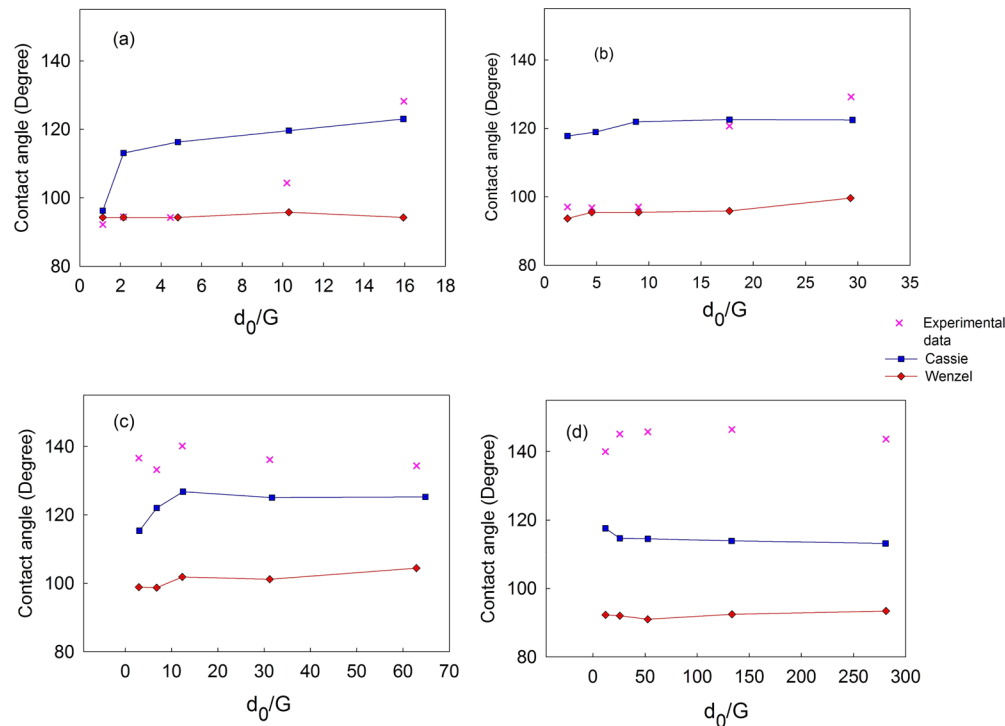


Figure 12. The apparent contact angle as a function of the ratio of the basal length of the drop profile d_0 to the groove width G for different drop volumes on a hydrophobic substrate (ppHex); (a) 0.4 nL, (b) 12 nL, (c) 40 nL, and (d) 4.5 μ L. Predictions of the model are compared to experimental data.⁵⁴

contact-angle measurements made from a parallel view of the droplet.

Figure 12 presents a comparison of the measured contact angles for different-sized water droplets on ppHex to the predictions of our model for the Cassie and Wenzel configurations on a surface characterized by the same values of \bar{G} , \bar{H} , \bar{W} , and θ_e as in the experiments. For this comparison, we use the basal length of the drop profile in the parallel view, d_0 , to scale the geometrical parameters of the surface, as was done in the experiments. According to our model, the Wenzel mode is the lowest-energy state for all of the cases shown in Figure 12.

For small droplets [Figure 12a and b], the experimental contact angles agree well with those predicted for the Wenzel mode for small values of d_0/G , and those predicted for the Cassie mode for large values of d_0/G . Although the Wenzel mode is energetically preferred, it is possible that the Cassie mode is metastable and long-lived in the experiments. Even though the Cassie mode is not the lowest-energy state, our

model can predict the correct contact angle, especially if the Bond number is small. With increasing drop size [Figure 12c and d], the experimentally measured contact angles become increasingly larger than those predicted by the model. This is likely because our assumption of a constant-curvature drop profile is no longer valid for these drops. The Bond numbers associated with the experiments range from 2.8×10^{-4} for the smallest (0.4 nL) drops to about 0.14 for the largest (4.5 μ L) drops. As can be seen in Table 1, gravity has a non-negligible effect on the contact angles predicted by our model at Bond numbers as small as 10^{-2} . Although the model predictions presented in Figure 12 correspond to nonzero values of the Bond number, we do not account for the effect of gravity-induced shape deformation on the equilibrium drop configuration. Thus, our model under-predicts contact angles for large drops with significant Bond numbers.

CONCLUSION

We presented a mathematical model based on free-energy minimization to predict the equilibrium wetting state of a two-dimensional liquid droplet on a periodically grooved solid surface. The relationship between the resulting contact angle and the geometry of the surface has been established for different droplet configurations, and the effect of drop size on the equilibrium contact angle has been described in terms of the Bond number. For small droplets (characterized by Bond numbers much smaller than unity), the relationship between contact angle and drop size is nonmonotonic. However, if the geometrical parameters characterizing the surface are scaled with the drop radius, the contact angle becomes independent of the scaled geometry. We used our model to construct phase diagrams depicting the dependence of the wetting configurations and their corresponding contact angles on geometrical parameters describing the surface. The resulting wetting phase diagrams and contact-angle isocontours can serve as guidelines for designing surfaces with desired wettability. Interestingly, we find the largest contact angles when the size of the drop is comparable to the length scales characterizing the surface topology.

While the contact angles predicted by our model exhibit some of the qualitative trends in the Cassie and Wenzel models, significant quantitative differences occur. As compared to the Cassie and Wenzel models, the main advantages of our model are (i) it provides a more detailed description of droplet wetting configurations, and (ii) it accounts for pinning/depinning of the contact line at step edges. Analysis of our detailed model indicates that contact-line pinning is essential for achieving large contact angles. The predictions of our continuum-level theoretical model are in good agreement with corresponding results from nanometer-scale MD simulations. Our contact-angle predictions are also in good agreement with experimentally measured contact angles of small drops, for which gravity-induced interface deformation is negligible.

AUTHOR INFORMATION

Corresponding Author

*E-mail: fichtthorn@psu.edu.

Notes

The authors declare no competing financial interest.

ACKNOWLEDGMENTS

This work was supported by the National Science Foundation, grant no. CBET 0730987.

REFERENCES

- (1) Feng, L.; Li, S.; Li, Y.; Li, H.; Zhang, L.; Zhai, L.; Song, L.; Liu, B.; Liang, L.; Zhu, D. Super-hydrophobic surfaces: From natural to artificial. *Adv. Mater.* **2002**, *14*, 1857–1860.
- (2) Roach, P.; Shirtcliffe, N. J.; Newton, M. I. Progress in superhydrophobic surface development. *Soft Matter* **2008**, *4*, 224–240.
- (3) Barthlott, W.; Neinhuis, C. Purity of the sacred lotus, or escape from contamination in biological surfaces. *Planta* **1997**, *202*, 1–8.
- (4) Neinhuis, C.; Barthlott, W. Characterization and distribution of water-repellent, self-cleaning plant surfaces. *Ann. Bot.* **1997**, *79*, 667–677.
- (5) Yan, Y. Y.; Gao, N.; Barthlott, W. Mimicking natural superhydrophobic surfaces and grasping the wetting process: A review on recent progress in preparing superhydrophobic surfaces. *Adv. Colloid Interface Sci.* **2011**, *169*, 80–105.
- (6) Bhushan, B. Bioinspired structured surfaces. *Langmuir* **2012**, *28*, 1698–1714.
- (7) Lau, K. K. S.; Bico, J.; Teo, K. B. K.; Chhowalla, M.; Amarutunga, G. A. J.; Milne, W. I.; McKinley, G. H.; Gleason, K. K. Superhydrophobic carbon nanotube forests. *Nano Lett.* **2003**, *3*, 1701–1705.
- (8) Feng, X.; Jiang, L. Design and creation of superwetting/antiwetting surfaces. *Adv. Mater.* **2006**, *18*, 3063–3078.
- (9) Zhai, L.; Berg, M. C.; Cebeci, F. Ç.; Kim, Y.; Milwid, J. M.; Rubner, M. F.; Cohen, R. E. Patterned superhydrophobic surfaces: Toward a synthetic mimic of the namib desert beetle. *Nano Lett.* **2006**, *6*, 1213–1217.
- (10) Jung, Y. C.; Bhushan, B. Mechanically durable carbon nanotube-composite hierarchical structures with superhydrophobicity, self-cleaning, and low-drag. *ACS Nano* **2009**, *3*, 4155–4163.
- (11) Kwon, Y.; Patankar, N. A.; Choi, J.; Lee, J. Design of surface hierarchy for extreme hydrophobicity. *Langmuir* **2009**, *25*, 6129–6136.
- (12) Ebert, D.; Bhushan, B. Durable Lotus-effect surfaces with hierarchical structure using micro- and nanosized hydrophobic silica particles. *J. Colloid Interface Sci.* **2012**, *368*, 584–591.
- (13) Lafuma, A. Quéré superhydrophobic states. *Nat. Mater.* **2003**, *2*, 457–460.
- (14) He, B.; Patankar, N. A.; Lee, J. Multiple equilibrium droplet shapes and design criterion for rough hydrophobic surfaces. *Langmuir* **2003**, *19*, 4999–5003.
- (15) Gao, L.; McCarthy, T. J. The “Lotus effect” explained: Two reasons why two length scales of topography are important. *Langmuir* **2006**, *22*, 2966–2967.
- (16) Barbieri, L.; Wagner, E.; Hoffmann, P. Water wetting transition parameters of perfluorinated substrates with periodically distributed flat-top microscale obstacles. *Langmuir* **2007**, *23*, 1723–1734.
- (17) Dorrer, C.; Rühle, J. Condensation and wetting transitions on microstructured ultrahydrophobic surfaces. *Langmuir* **2007**, *23*, 3820–3824.
- (18) Gao, L.; McCarthy, T. J. How Wenzel and Cassie were wrong. *Langmuir* **2007**, *23*, 3762–3765; *Langmuir* **2007**, *23*, 3762–3765.
- (19) Spori, D. M.; Drobek, T.; Zürcher, T. S.; Ochsner, M.; Sprecher, C.; Mühlebach, A.; Spencer, N. D. Beyond the lotus effect: Roughness influences on wetting over a wide surface-energy range. *Langmuir* **2008**, *24*, 5411–5417.
- (20) Jung, Y. C.; Bhushan, B. Wetting behaviour during evaporation and condensation of water microdroplets on superhydrophobic patterned surfaces. *J. Microsc.* **2008**, *229*, 127–140.
- (21) Cansoy, C. E.; Erbil, H. Y.; Akar, O.; Akin, T. Effect of pattern size and geometry on the use of Cassie-Baxter equation for superhydrophobic surfaces. *Colloids Surf., A* **2011**, *386*, 116–124.
- (22) Liu, G.; Fu, L.; Rode, A. V.; Craig, V. S. J. Water droplet motion control on superhydrophobic surfaces: Exploiting the Wenzel-to-Cassie transition. *Langmuir* **2011**, *27*, 2595–2600.
- (23) Wenzel, R. N. Resistance of solid surfaces to wetting by water. *Ind. Eng. Chem.* **1936**, *28*, 988–994.
- (24) Cassie, A. B. D.; Baxter, S. Wettability of porous surfaces. *Trans. Faraday Soc.* **1944**, *40*, 546–551.
- (25) Wolansky, G.; Marmur, A. Apparent contact angles on rough surfaces: The Wenzel equation revisited. *Colloids Surf., A* **1999**, *156*, 381–388.
- (26) Brandon, S.; Haimovich, N.; Yeager, E.; Marmur, A. Partial wetting of chemically patterned surfaces: The effect of drop size. *J. Colloid Interface Sci.* **2003**, *263*, 237–243.
- (27) Marmur, A.; Bittoun, E. When Wenzel and Cassie are right: Reconciling local and global considerations. *Langmuir* **2009**, *25*, 1277–1281.
- (28) Yang, Tartaglino, C. U.; Persson, B. N. J. Influence of surface roughness on superhydrophobicity. *Phys. Rev. Lett.* **2006**, *97*, 116103.
- (29) Lundgren, M.; Allan, N. L.; Cosgrove, T. Modeling of wetting: A study of nanowetting at rough and heterogeneous surfaces. *Langmuir* **2007**, *23*, 1187–1194.

- (30) Wu, H.; Borhan, A.; Fichthorn, K. A. Coarse-grained interaction of a fluid with a physically-patterned solid surface: Application to nanodroplet wetting. *J. Low Temp. Phys.* **2009**, *157*, 277–295.
- (31) Gross, M.; Varnik, F.; Raabe, D.; Steinbach, I. Small droplets on superhydrophobic substrates. *Phys. Rev. E* **2010**, *81*, 051606.
- (32) Extrand, C. W. Modeling of ultralyophobicity: Suspension of liquid drops by a single asperity. *Langmuir* **2005**, *21*, 10370–10374.
- (33) Tóth, T.; Ferraro, D.; Chiarello, E.; Pierno, M.; Mistura, G.; Bissacco, G.; Sempredon, C. Suspension of water droplets on individual pillars. *Langmuir* **2011**, *27*, 4742–4748.
- (34) Patankar, N. A. Transition between superhydrophobic states on rough surfaces. *Langmuir* **2004**, *20*, 7097–7102.
- (35) Ishino, C.; Okumura, L.; Quéré, D. Wetting transitions on rough surfaces. *Europhys. Lett.* **2004**, *68*, 419–425.
- (36) Li, W.; Amirfazli, A. A thermodynamic approach for determining the contact angle hysteresis for superhydrophobic surfaces. *J. Colloid Interface Sci.* **2005**, *292*, 195–201.
- (37) Li, W.; Amirfazli, A. Microtextured superhydrophobic surfaces: A thermodynamic analysis. *Adv. Colloid Interface Sci.* **2007**, *132*, 51–68.
- (38) Sheng, Y.-J.; Jiang, S.; Tsao, H.-K. Effects of geometrical characteristics of surface roughness on droplet wetting. *J. Chem. Phys.* **2007**, *127*, 234704.
- (39) Whyman, G.; Bormashenko, E. How to make the Cassie wetting state stable? *Langmuir* **2011**, *27*, 8171–8176.
- (40) Bormashenko, E.; Musin, A.; Whyman, G.; Zinigrad, M. Wetting transitions and depinning of the triple line. *Langmuir* **2012**, *28*, 3460–3464.
- (41) Chen, Y.; He, B.; Lee, J.; Patankar, N. A. Anisotropy in the wetting of rough surfaces. *J. Colloid Interface Sci.* **2005**, *281*, 458–464.
- (42) Chatain, D.; Lewis, D.; Baland, J.-P.; Carter, W. C. Numerical analysis of the shapes and energies of droplets on micropatterned substrates. *Langmuir* **2006**, *22*, 4237–4243.
- (43) Koishi, T.; Yasuoka, K.; Fujikawa, S.; Ebisuzaki, T.; Zeng, X. C. Coexistence and transition between Cassie and Wenzel state on pillared hydrophobic surface. *Proc. Natl. Acad. Sci. U.S.A.* **2009**, *106*, 8435–8440.
- (44) DeConinck, J.; Dunlop, F.; Huillet, T. Metastable wetting. *J. Stat. Mech.* **2011**, P06013.
- (45) Patankar, N. A. On the modeling of hydrophobic contact angles on rough surfaces. *Langmuir* **2003**, *19*, 1249–1253.
- (46) Marmur, A. Wetting on hydrophobic rough surfaces: To be heterogeneous or not to be? *Langmuir* **2003**, *19*, 8343–8348.
- (47) Extrand, C. W.; Moon, S. I. When sessile drops are no longer small: Transitions from spherical to fully flattened. *Langmuir* **2010**, *26*, 11815–11822.
- (48) Vergauwe, N.; Witters, D.; Ceyssens, F.; Vermeir, S.; Verbruggen, B.; Puers, R.; Lammertyn, J. A versatile electrowetting-based digital microfluidic platform for quantitative homogeneous and heterogeneous bio-assays. *J. Micromech. Microeng.* **2011**, *21*, 054026.
- (49) Lee, C. Y.; Lin, Y. H.; Lee, G. B. A droplet-based microfluidic system capable of droplet formation and manipulation. *Microfluid. Nanofluid.* **2009**, *6*, 599–610.
- (50) Zeng, J.; Korsmeyer, T. Principles of droplet electrohydrodynamics for lab-on-a-chip. *Lab Chip* **2004**, *4*, 265–277.
- (51) Wu, H.; Borhan, A.; Fichthorn, K. A. Interaction of fluids with physically patterned solid surfaces. *J. Chem. Phys.* **2010**, *133*, 054704.
- (52) Young, X.; Zhang, L. T. Nanoscale wetting on groove-patterned surfaces. *Langmuir* **2009**, *25*, 5045–5053.
- (53) Wolf, F. G.; dos Santos, L. O. E.; Philippi, P. C. Modeling and simulation of the fluid-solid interaction in wetting. *J. Stat. Mech.: Theory Exp.* **2009**, P06008.
- (54) Yang, J.; Rose, F. R. A. J.; Gadegaard, N.; Alexander, M. R. Effect of sessile drop volume on the wetting anisotropy observed on grooved surfaces. *Langmuir* **2009**, *25*, 2567–2571.